Multiwavelength investigation of a near-solar metallicity sub-DLA at $z_{\rm abs} = 1.3647$ towards PKS 0237-233[⋆]

Raghunathan Srianand[1], Neeraj Gupta[2], Patrick Petitjean[3,4]

[1] IUCAA, Post Bag 4, Ganeshkhind, Pune 411 007, India
   email: anand@iucaa.ernet.in
[2] NCRA, Post Bag 3, Ganeshkhind, Pune 411 007, India
   email:neeraj@ncra.tifr.res.in
[3] Institut d'Astrophysique de Paris – Université Pierre et Marie Curie, 98bis Boulevard Arago, F-75014 Paris, France
[4] LERMA, Observatoire de Paris, 61 Rue de l'Observatoire, F-75014 Paris, France
   email:petitjean@iap.fr

ABSTRACT

We searched for 21-cm absorption associated with the $z_{\rm abs}$= 1.3647 absorption system toward the gigahertz peaked-spectrum source PKS 0237−233 using the Giant Metrewave Radio Telescope. A high quality UVES spectrum shows that C I and C I* are detected at this redshift together with C II*, Mg I, Mg II, Si II, Al II, Fe II and Mn II. The complex profiles, spread over $\sim$ 300 km s^{-1}, are fitted with 21 Voigt profile components. None of these components are detected in 21-cm absorption down to a detection limit of $\tau(3\sigma) \leqslant 3 \times 10^{-3}$ (or $N({\rm H~I})/T_{\rm S} \leqslant 10^{17}$ cm^{-2} K^{-1}). We derive $\log [N({\rm H~I})$ cm$^{-2}] \leqslant 19.30 \pm 0.30$ using the Lyα absorption line detected in the IUE spectrum of the quasar. Mg II, Si II and Al II column densities are consistent with near solar metallicity and we measure [O/H] $\geqslant -0.33$. Using photoionization models constrained by the fine-structure excitations of C I and C II, and the 21-cm optical depth, we show that the C I absorption arises predominantly either in a warm ionized medium (WIM) or warm neutral medium (WNM) in ionization and thermal equilibrium with the meta-galactic UV background dominated by QSOs and star forming galaxies. The estimated thermal pressure of the gas is of the same order of magnitude over different velocity ranges through the absorption profile ($2.6 \leqslant \log[P/k({\rm cm}^{-3}{\rm K})] \leqslant 4.0$). The gas-phase metallicity corrected for ionization is Z $\geqslant 0.5$ Z$_\odot$ with a signature of iron co-production elements being under abundant compared to $\alpha-$process elements by $\sim$0.5 dex. At $z_{\rm abs} \geqslant 1.9$, C I absorption is usually associated with H$_2$ absorption arising from cold gas in damped Lyman-α systems. This system and the $z_{\rm abs} = 2.139$ toward Tol 1037−270 are the only two systems known which show that C I absorption can also be detected in warm gas provided the metallicity is high enough. Interestingly, both the systems are part of unusual concentrations of absorption lines.

Key words: Quasars: absorption lines – Quasars: individual: PKS 0237−233

1 INTRODUCTION

The diffuse gas in the interstellar medium (ISM) is known to exhibit a wide range of physical conditions (temperature, density, radiation field and chemical composition). These physical quantities are influenced by the local star formation, the cosmic ray energy density, photoelectric heating

by dust as well as mechanical energy input from both impulsive disturbances such as supernova explosions (McKee & Ostriker, 1977) as well as more steady injection of energy in the form of winds from stars (Abbott, 1982). Understanding these physical conditions and the processes that maintain these conditions are important for our understanding of galaxies and their evolution.

The relative populations of the ground and excited levels of C I have been used to discuss the particle density, the ambient UV radiation field and the temperature of the cosmic-microwave background radiation (see Bahcall, Joss

---

[⋆] Based on observations carried out at the European Southern Observatory with UVES in the course of the Large Program "The Cosmic Evolution of the IGM" 166.A-0106 on the 8.2 m VLT telescopes Kuyen operated at Paranal Observatory; Chile.

& Lynds 1973; Meyer et al., 1986; Songaila et al. 1994; Ge, Bechtold & Black, 1997; Roth & Bauer, 1999; Srianand et al. 2000; Silva & Viegas, 2002). In the Galactic ISM, fine-structure excitation of C I has been used to study the distribution of thermal pressure (see Jenkins & Tripp 2001). At high redshifts C I absorption is very rare and detected in only a handful of systems ($\simeq 15\%$ of the damped Lyman α systems (DLAs) at $z_{abs} \geqslant 1.9$). Usually, C I absorption in these systems is closely associated with low temperature, high density gas that often shows associated H_2 absorption (Ge & Bechtold, 1999; Petitjean et al. 2000; Ledoux, Petitjean & Srianand 2003; Srianand et al. 2005). The only exception is the $z_{abs} = 2.139$ system towards Tol 1037−270 (Srianand & Petitjean, 2001) that originates from a solar metallicity sub-DLA (i.e. systems that show damping wings with log N(H I)< 20.3) very much similar to the one we shall discuss here in which the absence of detectable H_2 absorption lines suggests that the gas temperature is probably high.

Like C I, C II* absorption has been detected in every system where H_2 is present (Srianand et al. 2005). However, C II* has also been seen in a considerable fraction of DLAs ($\simeq 50\%$) without H_2 (Wolfe, Prochaska & Gawiser 2003; Wolfe, Gawiser & Prochaska 2003; Srianand et al. 2005). It has been found that C II* absorption is always detected when log N(H I) $\geqslant 21$ and also in systems with high metallicity irrespective of N(H I). As C II* is an important coolant of the ISM, the corresponding C II* column density can be used to discuss the cooling rate in the absorbing gas (Wolfe et al. 2004).

The nature and physical conditions in the H I gas can also be probed by 21-cm absorption lines. The searches for 21-cm absorption in DLAs at $z_{abs} \geqslant 2$ have mostly resulted in null detections with typical spin temperatures $\geqslant 10^3$ K (see Table 3 of Kanekar & Chengalur 2003 and Table 1 of Curran et al. 2005). Based on the lack of 21-cm and H_2 absorption in most of the systems it has been inferred that most of DLAs actually trace a warm neutral phase (see also Petitjean, Srianand & Ledoux 2000). However one of the possible uncertainties to interpret the 21 cm data could be the unknown covering factor of the H I gas in front of the radio source (see Briggs & Wolfe 1983 for a discussion).

Despite obvious advantages of studying all the above indicators simultaneously, such studies are possible only for a few systems [at $z_{abs} = 2.8110$ towards PKS 0528−250 (Carilli et al., 1996; Srianand & Petitjean 1998), $z_{abs} = 1.944$ towards Q1157+014 (Wolfe & Briggs 1981; Srianand et al. 2005) and $z_{abs} = 2.03954$ towards PKS 0458−020 (Wolfe et al. 1985; Briggs et al 1989; Heinmüller et al. 2005)]. This is mainly because only a small fraction of the QSOs with interesting DLAs are radio-loud and, the redshifted 21-cm frequency range in many cases is not covered by the present-day radio telescopes or is affected by strong radio frequency interferences.

The UVES spectrum of the compact source PKS 0237−233, that was obtained as part of the ESO-VLT large programme "The Cosmic Evolution of the IGM" (Bergeron et al. 2004), shows C I, C I* and C II* absorption lines spread over ~ 300 km s^{-1} in a strong Mg II sub-DLA system at $z_{abs} = 1.365$. The wavelength range into which the corresponding 21-cm absorption is redshifted can be covered by the Giant Metrewave Radio Telescope (GMRT)

610 MHz band. Here, we present the analysis of this system using the high-resolution optical spectrum obtained with UVES/VLT, a low-resolution UV spectra obtained with IUE and the GMRT radio spectrum covering the redshifted 21-cm absorption.

2   OBSERVATIONS AND DATA REDUCTION

2.1   Optical UVES observations

The optical spectrum of PKS 0237−233 used in this study was obtained using the Ultraviolet and Visible Echelle Spectrograph (UVES; Dekker et al. 2000) mounted on the ESO Kueyen 8.2 m telescope at the Paranal observatory in the course of the ESO-VLT large programme "The Cosmic Evolution of the IGM". PKS 0237−233 was observed through a 1″ slit (with a seeing typically $\leqslant 0.8$ ″) for ~ 12 hr with central wavelengths adjusted to 3460Å and 5800Å in the blue and red arms, respectively, using dichroic no. 1 and for another ~ 14 hr with central wavelengths at 4370Å and 8600Å in the blue and red arms with dichroic no. 2. The raw data were reduced using the latest version of the UVES pipeline (Ballester et al. 2000) which is available as a dedicated context of the MIDAS data reduction software. The main function of the pipeline is to perform a precise inter-order background subtraction for science frames and master flat-fields, and to allow an optimal extraction of the object signal, rejecting cosmic ray impacts and performing sky-subtraction at the same time. The reduction is checked step by step. Wavelengths are corrected to vacuum-heliocentric values and individual 1D spectra are combined. Air-vacuum conversions and heliocentric corrections were done using standard conversion equations (Edlèn 1966; Stumpff 1980). Addition of individual exposures is performed using a sliding window and weighting the signal by the errors in each pixel. Great care was taken in computing the error spectrum while combining the individual exposures. Our final error is the quadratic sum of appropriately interpolated weighted mean errors and possible errors due to scatter in the individual flux measurements. The final combined spectrum covers the wavelength range of 3000-10,000Å. A typical S/N ~ 60-80 per pixel (of 0.035 Å) is achieved in the whole wavelength range of interest. The detailed quantitative description of data calibration is presented in Aracil et al. (2004) and Chand et al. (2004).

2.2   Radio Observations

The radio spectrum was obtained on 2004, Feb 9 using GMRT. The local oscillator chain was tuned to centre the baseband at the corresponding redshifted 21-cm frequency. The FX correlator system at GMRT splits the baseband into 128 channels, yielding a velocity resolution of 3.9 km s^{-1} for our chosen baseband bandwidth of 1 MHz. We observed standard flux calibrators 3C48 or 3C147 every two hours to correct for the amplitudes and bandpass variations. Since the background radio source, PKS 0237−233 is unresolved for the GMRT array at the observing frequency, observing a separate phase calibrator was not required. A total 8 hrs of on-source data were acquired in both the circular polarization channels RR and LL.
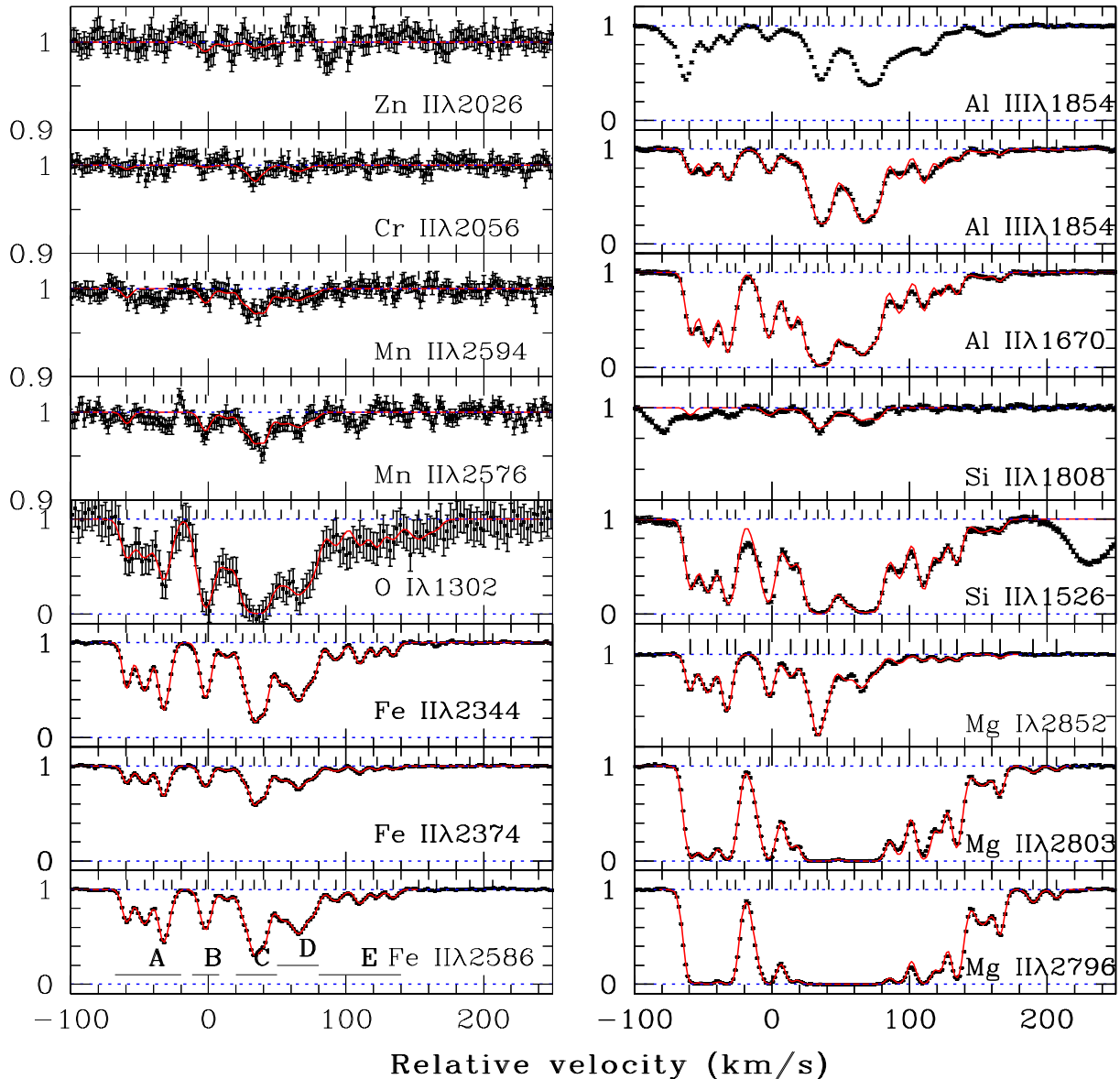
Figure 1. Velocity plots of the absorption line system centered at $z_{abs} = 1.3647$. The points with error bars are the observations and the continuous curve shows the Voigt profile fit to the absorption profiles. Tick marks in each panel indicate the location of individual components. We identify 21 distinct components based on the fits to Mg II and Fe II profiles. The distinct velocity ranges discussed in detail in the text are indicated in the bottom left panel.

The radio data were reduced in the standard way using the Astronomical Image Processing System (NRAO AIPS package). After the initial flagging and calibration, source and calibrator data were examined to flag and exclude the baselines and timestamps affected by Radio Frequency Interference (RFI). It was noticed that data on 3C 147 was not particularly good as compared to 3C 48. Of the 4 time-scans (exposures) on 3C 48 and 3C 147, 3C147 contributed only to the last one. So we used only 3C 48 for the band-pass calibration. Applying these complex gains and band-

pass, a continuum map of the source was made using line free channels. Using this map as a model, self-calibration complex gains were determined and applied to all the frequency channels. The same continuum map was then used to subtract the continuum emission (a flux density of 5.1 Jy). The continuum subtracted data set was then imaged separately in stokes RR and LL to get three-dimensional (with third axis as frequency) data cubes. Spectra at the quasar position were extracted from these cubes and compared for consistency. The two polarization channels were then com-
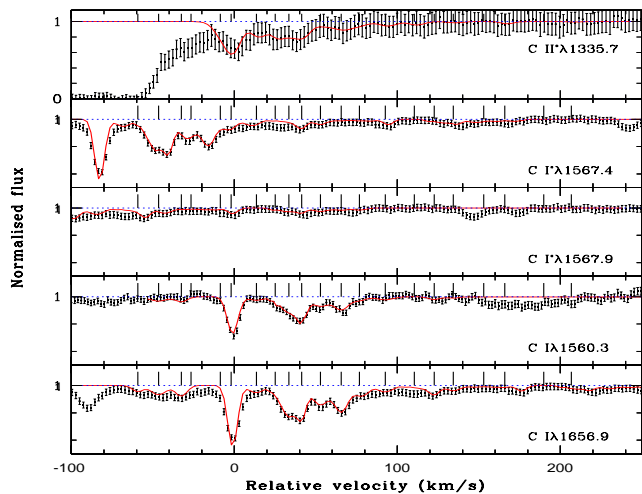
Figure 2. Excited fine-structure lines of C I and C II plotted on a velocity scale with respect to $z_{\mathrm{abs}}= 1.3647$. Points with errorbars are the observed data and the best fit is shown as a continuous curve. The tick marks indicate the location of distinct Voigt profile components.

Figure 3. Top panel shows the low resolution ($\simeq 5.5$ Å) IUE spectrum of PKS 0237−233, the fitted continuum (smooth continuous curve) and the error spectrum (dashed line). The expected positions of the Lyman series lines at $z_{\mathrm{abs}}= 1.3647$ are marked by vertical lines. Single component Voigt profile fits for log N (H I) = 19, 19.5 and 20.0 are shown by, respectively, continuous, dotted and dashed profiles. These fits suggest that the system is a sub-DLA with log N(H I) $\leqslant 20.0$.

bined to derive the final stokes I spectrum, which was then shifted to heliocentric frame.

2.3   IUE spectrum

An IUE spectrum of PKS 0237−233 was obtained by Richard F. Green as part of an observing programme to study high-redshift quasars (IUE Program ID: QSDRG and IUE image number: LWR10935). The spectrum was obtained with the large aperture (approximately 10 x 20 arc sec) and an exposure time of 25,800 s. The typical spectral resolution is ~ 6 Å and the signal to noise per pixel ~ 5. We used the pipeline calibrated IUE spectra obtained directly from Multimission Archive at Space Telescope (MAST).

3 $z_{\mathrm{abs}}= 1.3647$ SYSTEM

3.1   Neutral and singly ionized species

The velocity profiles of some of the neutral and singly ionized species seen at $z_{\mathrm{abs}}= 1.3647$ together with a multicomponent Voigt profile fit are shown in Fig 1. They are spread over $\simeq 300$ km s^{-1}. The absorption lines of Mg I, Si II, Al II, Al III and Fe II fall in the spectral range with the best signal-to-noise ratio. We also detect O Iλ1302 in the blue part of the UVES spectrum that has a lower SNR. Weak Mn II lines are clearly detected in the strongest Mg II components corresponding to velocity ranges B and C (see left bottom panel in Fig. 1). We also tentatively detect Cr II in the same components (see Fig. 1).

We detect C I, C I* and C II* absorption in most of the components (see Fig. 2). Simultaneous Voigt profile fitting of all the metal transitions requires 21 independent components. The results are summarised in Table. 1. To facilitate the discussion, we divide the velocity profiles into 5 distinct
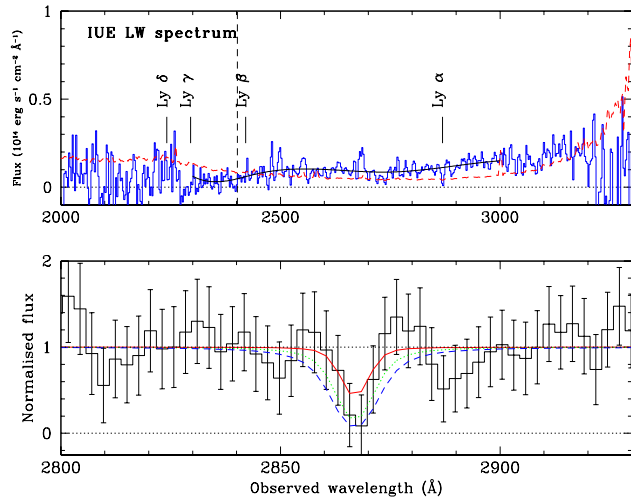
velocity regions marked as A, B, C, D and E in the bottom left panel of Fig. 1. The integrated column densities of different species within these velocity ranges are reported in Table 1. Ni IIλ1709, Co IIλ1466, Na I$\lambda\lambda$3303.3,3303.9, Ca II$\lambda\lambda$3934,3969 are not detected, nor are the fine-structure lines of O I and Si II.

3.2   Constraints on the total $N(\mathbf{H\ I})$

We used the IUE LW spectrum from the IUE archive to derive the total H I column density, $N(\mathrm{H\ I})$. We detect a line at the expected position of the redshifted Lyα absorption with rest equivalent width 3.0 ± 1.0Å (Fig. 3). If we assume the absorption to be in the damped portion of the curve of growth we derive log N (H I) = 19.30±0.30. This means that N(H I) in individual components cannot be higher than this value. If the Lyα line is the blend of saturated Lyα absorptions from individual metal-line components, then the total N(H I) could be less than this value.

The derived constraint on N(H I) is consistent with ASCA & ROSAT observations that do not detect excess soft X-ray absorption on top of the galactic absorption (Yamasaki et al. 1998). Thus, the allowed range in N(H I) is very much consistent with the system being either a sub-DLA or a high column density Lyman Limit system. Upper limits on N(H I) in the individual components can be obtained from our GMRT spectrum for an assumed spin-temperature (T_{S}). The GMRT spectrum is shown in the upper panel of Fig. 4. Despite reaching a 1σ limit of 10^{-3} for τ(21 cm) we do not detect any absorption at the expected positions of the different individual components detected in the UV spectrum of neutral and/or singly ionized species.

The neutral hydrogen column density in a velocity in-

Table 1. Voigt profile fitting results for individual components:[1]

$z_{\rm abs}$	b(km/s)	N(Mg I)	N(Mg II)	N(O I)	N(Si II)	N(Fe II)	N(C II*)	N(C I)	N(C I*)	N(H I)[2]
				Velocity range A						
1.364232	2.6(0.2)	11.21(0.01)	13.97(0.01)	13.58(0.08)	13.58(0.02)	12.89(0.01)	b	11.80(0.19)	$\leqslant 12.00$	$\leqslant 18.36$
1.364334	5.1(0.2)	11.38(0.01)	13.47(0.01)	13.62(0.06)	13.56(0.01)	13.04(0.01)	b	12.12(0.10)	$\leqslant 12.00$	$\leqslant 18.66$
1.364443	3.0(0.2)	11.50(0.01)	13.73(0.02)	13.93(0.09)	13.77(0.02)	13.21(0.01)	b	12.07(0.12)	$\leqslant 12.00$	$\leqslant 18.43$
1.364490	2.1(0.7)	10.00(0.10)	12.56(0.01)	12.85(0.31)	13.04(0.02)	12.21(0.06)	b	$\leqslant 11.70$	$\leqslant 12.00$	$\leqslant 18.30$
Total		11.86(0.01)	14.26(0.01)	14.23(0.05)	14.16(0.01)	13.56(0.01)	b	12.49(0.07)	$\leqslant 12.30$	$\leqslant 19.21$
				Velocity range B						
1.364632	5.1(0.1)	9.32(0.65)	12.46(0.01)	$\leqslant 13.0$	13.03(0.01)	$\leqslant 11.50$	12.82(0.06)	$\leqslant 11.70$	$\leqslant 12.00$	$\leqslant 18.66$
1.364685	4.0(0.1)	11.37(0.01)	13.46(0.01)	14.80(0.16)	13.69(0.01)	13.07(0.01)	13.13(0.04)	12.92(0.01)	12.26(0.02)	$\leqslant 18.56$
Total		11.37(0.01)	13.50(0.01)	14.80(0.16)	13.77(0.01)	13.07(0.01)	13.30(0.03)	12.92(0.01)	12.26(0.02)	$\leqslant 19.07$
				Velocity range C						
1.364807	4.7(0.5)	11.09(0.01)	13.00(0.00)	13.73(0.08)	13.18(0.01)	12.40(0.03)	12.83(0.04)	11.98(0.05)	$\leqslant 12.00$	$\leqslant 18.62$
1.364897	2.5(0.7)	10.97(0.01)	14.31(0.03)	14.31(0.27)	13.60(0.02)	12.62(0.10)	12.72(0.07)	11.71(0.25)	$\leqslant 12.00$	$\leqslant 18.34$
1.364963	4.2(0.6)	11.75(0.01)	13.41(0.09)	14.46(0.47)	14.14(0.02)	13.40(0.04)	12.73(0.07)	12.63(0.01)	12.10(0.07)	$\leqslant 18.57$
1.365025	2.9(0.4)	11.21(0.01)	14.16(0.18)	15.06(0.49)	13.87(0.02)	13.12(0.06)	12.71(0.07)	12.55(0.03)	11.97(0.11)	$\leqslant 18.41$
Total		11.97(0.01)	14.59(0.07)	15.23(0.34)	14.43(0.01)	13.65(0.03)	13.35(0.03)	12.97(0.02)	12.35(0.08)	$\leqslant 19.26$
				Velocity range D						
1.365116	5.4(0.7)	11.14(0.01)	13.42(0.06)	13.87(0.08)	13.62(0.01)	12.93(0.06)	12.26(0.16)	12.43(0.02)	12.34(0.02)	$\leqslant 18.69$
1.365217	6.8(0.7)	11.38(0.01)	14.16(0.80)	14.14(0.05)	14.06(0.01)	13.25(0.04)	12.63(0.08)	12.57(0.01)	$\leqslant 12.00$	$\leqslant 18.78$
1.365305	3.9(0.4)	10.78(0.02)	13.99(0.02)	13.68(0.08)	13.83(0.02)	12.69(0.07)	12.04(0.24)	11.96(0.04)	11.96(0.05)	$\leqslant 18.54$
Total		11.64(0.01)	14.43(0.43)	14.41(0.04)	14.35(0.01)	13.50(0.03)	12.85(0.07)	12.86(0.01)	12.49(0.03)	$\leqslant 19.31$
				Velocity range E						
1.365430	5.4(0.3)	10.70(0.02)	13.20(0.00)	13.42(0.08)	13.37(0.01)	12.51(0.01)	12.28(0.15)	11.95(0.06)	$\leqslant 12.00$	$\leqslant 18.69$
1.365570	3.9(0.2)	10.48(0.03)	13.69(0.01)	13.37(0.09)	13.52(0.01)	12.52(0.01)	12.11(0.19)	$\leqslant 11.70$	$\leqslant 12.00$	$\leqslant 18.55$
1.365667	2.5(0.6)	10.43(0.04)	12.74(0.00)	13.37(0.10)	13.04(0.01)	12.19(0.03)	$\leqslant 12.00$	$\leqslant 11.70$	$\leqslant 12.00$	$\leqslant 18.35$
1.365759	3.3(0.4)	10.43(0.04)	13.11(0.01)	13.19(0.10)	13.10(0.01)	12.24(0.02)	11.64(0.54)	$\leqslant 11.70$	$\leqslant 12.00$	$\leqslant 18.46$
Total		11.12(0.01)	13.92(0.01)	13.95(0.05)	13.90(0.01)	12.99(0.01)	12.56(0.14)	....	....	$\leqslant 19.29$
				Velocity range F						
1.365906	8.0(0.2)	$\leqslant 9.47$	12.21(0.01)	13.38(0.11)	12.65(0.02)	$\leqslant 11.50$	$\leqslant 12.00$	$\leqslant 11.70$	$\leqslant 12.00$	$\leqslant 18.86$
1.366008	1.8(0.1)	10.08(0.09)	12.13(0.01)	12.72(0.31)	12.30(0.05)	$\leqslant 11.50$	$\leqslant 12.00$	$\leqslant 11.70$	$\leqslant 12.00$	$\leqslant 18.21$
1.366197	3.5(0.4)	$\leqslant 9.47$	11.48(0.02)	$\leqslant 13.0$	$\leqslant 12.00$	$\leqslant 11.50$	$\leqslant 12.00$	$\leqslant 11.70$	$\leqslant 12.00$	$\leqslant 18.49$
1.366330	1.9(0.7)	$\leqslant 9.47$	11.23(0.02)	$\leqslant 13.0$	$\leqslant 12.00$	$\leqslant 11.50$	$\leqslant 12.00$	$\leqslant 11.70$	$\leqslant 12.00$	$\leqslant 18.23$

Velocity ranges are defined in Fig. 1.

[1] Column densities are given in logarithmic units.

[2] upper limit on N(H I) obtained from the GMRT spectrum assuming $T_{\rm S} = 100$ K; for higher $T_{\rm S}$ this should be multiplied by $(T_{\rm S}({\rm K})/100)$

b blended with other lines

terval v and $v+dv$ for an optically thin cloud is related to the optical depth, $\tau(v)$, and to the spin temperature ($T_{\rm S}$) by

$$N({\rm H\ I}) = 1.835 \times 10^{18}\ T_{\rm S} \int \tau(v)\ dv\ {\rm cm}^{-2} \quad (1)$$

If we assume the absorption line to have a perfect Gaussian profile with a peak optical depth $\tau_{\rm P}$, then the above equation will become,

$$N({\rm H\ I}) = 1.93 \times 10^{18}\ \tau_{\rm P}\ T_{\rm S}\ \Delta V\ {\rm cm}^{-2} \quad (2)$$

where $\Delta V = 2\sqrt{\ln 2} \times b$ is the FWHM of the Gaussian profile with b the Doppler parameter.

Note that the above equations assume the absorbing cloud to be homogeneous and to cover the background source completely. PKS 0237−233 is a very compact radio source that is not resolved in our GMRT observations. VLBA observations of this source at 2.32 and 8.55 GHz have revealed structures at milli-arcsec scales (Fey et al. 1996). Most of the flux is in two components that are roughly separated by $\sim$ 10 milli-arcsec (see also Fomalont et al. 2000). These components account for all the flux at 2.32 and 8.55 GHz implying there is no broad diffuse radio emission in this source. The strongest of these components has 60% of the flux at 2.32 GHz (Fey et al 1996) and 70% of the flux at 5 GHz (Famalont et al 2000). It has therefore a steep spectrum ($f_\nu \propto \nu^{-1.2}$) and probably dominates the flux at 610

MHz. The second brightest component has a flat spectrum ($f_\nu \propto \nu^{-0.2}$) and should correspond to the core of the radio source and therefore to the optical counterpart. If this is the case, then the optical and 610 MHz radio lines of sight are separated by 10 milli-arcsec. However, the spectral indices derived above are highly uncertain due to different beam sizes and component decompositions of the two above observations. Because of this, it is unclear which of these components is indeed associated with the optical point source and the angular separation of 10 milli-arcsec should be considered as an upper limit. One milli-arcsec at $z = 1.35$ corresponds to a linear size of 8.5 pc (for a flat universe with $\Omega_\Lambda = 0.73$, $\Omega_m = 0.27$, H$_0 = 71$ km/s/Mpc). This means the optical and radio sightlines are either coincident or separated by $\sim$85 pc.

Assuming that the velocity width of the H I feature is the same as that of metals, and using $\tau_{\rm P}(3\sigma) = 0.003$ and $T = 100$ K, as expected in the cold neutral medium, we derive upper limits on N(H I) in individual components. These values are listed in last column of Table. 1. These limits should be scaled up by $T_{\rm S}(K)/100$. Also for temperatures typical of the warm neutral medium (WNM) or warm ionized medium (WIM) of our Galaxy, higher b values (say 9 km s^{-1}) should be considered.

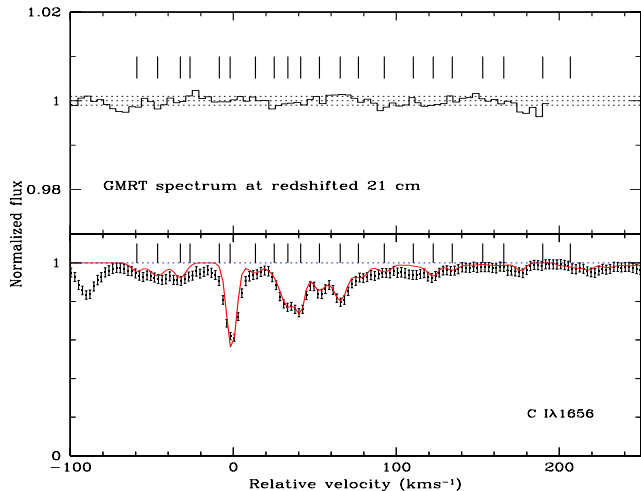It is clear that the uncertainties on the temperature and

Figure 4. Top panel shows the GMRT spectrum on a velocity scale centered at $z_{\rm abs} = 1.3647$. The horizontal dashed lines correspond to the mean and 1σ range in the normalised flux. The corresponding C Iλ1606 absorption is plotted in the bottom panel. Vertical tick marks show the location of different velocity components derived from the metal line profiles.
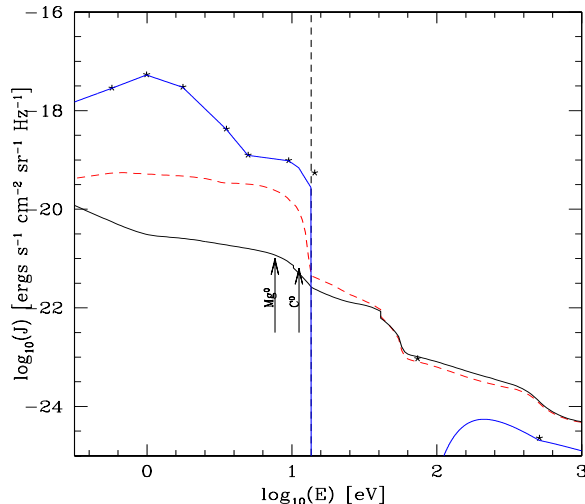

Figure 5. Input spectral energy distributions (SEDs) used in our model calculations. Continuous and dashed lines are SED taken from Haardt & Madau (2005) for the UV extra-galactic background contributed respectively by QSOs alone and QSOs and Lyman break galaxies. Stars indicate the Galactic UV background SED computed by Black (1987). The vertical dashed line shows the Lyman Limit; the ionization potentials of C^0 and Mg^0 are shown with arrows.

Table 2. Total column density:

Species	$\log N(\mathrm{cm}^{-2})$
N(H I)	19.30 ± 0.30
N(O I)	$\geqslant 15.46$
N(Mg I)	12.39 ± 0.00
N(Mg II)	$\geqslant 14.98$
N(C II*)	13.73 ± 0.02
N(Fe II)	14.13 ± 0.01
N(Si II)	14.89 ± 0.01
N(Al II)	$\geqslant 13.46$
N(Al III)	13.53 ± 0.01
N(Mn II)	11.81 ± 0.03
N(Cr II)	12.32 ± 0.13

the covering factor of the cloud in front of the radio-source prevents any rapid conclusion. To go further in the analysis of this system, in the following we construct photoionization models and constrain them using information from the 21 cm, Lyα , C I, C I* and C II* absorption lines.

4 MODEL CALCULATIONS

As the total $N(\mathrm{H\ I})$ in this system is less than 10^{20} cm^{-2}, it is most likely that ionization correction is important when deriving metallicity for most of the species. As an exception to this, O I and H I are coupled through charge-exchange reaction and for $N(\mathrm{H\ I}) \geqslant 10^{19}$ cm^{-2}, $N(\mathrm{O\ I})/N(\mathrm{H\ I})$ directly reflects [O/H] (see Viegas, 1995 and results presented below). As O Iλ1302 is possibly saturated in the central components (see Fig. 1) we can derive only a lower limit on $N(\mathrm{O\ I})$. We find [O/H]$\geqslant -0.33$ if we consider $\log N(\mathrm{H\ I}) \simeq$

19.3. High metallicity is also inferred from Mg II and Si II (see Table. 2). Clearly the gas under consideration must have gone through (or is going through) a prolonged period of vigorous star-formation activity.

To correct for ionization we use model calculations performed with the photoionization-simulation code CLOUDY (Ferland et al. 1998). Keeping in mind the preferred value $\log N(\mathrm{H\ I}) = 19.3 \pm 0.30$, we consider three total H I column densities, $\log N(\mathrm{H\ I}) = 19.0$, 19.5 and 20.0, at which the calculation is stopped. Relative metal abundances are considered solar and the total metallicity is $Z = 0.5\ Z_\odot$. This is motivated by the above inferred oxygen metallicity.

Most of the model calculations discussed below use a ionizing radiation spectrum that is a combination of the meta-galactic UV background at $z = 1.35$ contributed by QSOs and galaxies as computed by Haardt & Madau (2005) (dashed SED in Fig. 5) and the Cosmic Microwave Background with $T_{\rm CMBR} = 6.4$ K. Relative to quasars, galaxies contribute approximately an order of magnitude higher flux in the energy ranges corresponding to the ionization potentials of C^0 and Mg^0 (See also Wolfe et al. 2004). We also consider models with additional local radiation (continuous curve with points in Fig. 5). For this purpose we use the Black (1987) galactic background radiation after removing the H I ionizing photons as usually done in the case of ISM simulations (see e.g. Draine & Bertoldi, 1996; Shaw et al. 2006). We consider dust to metal ratio 1/10 of that observed in the Galactic ISM.

First we mainly focus our attention on models with meta-galactic radiation field contributed by QSOs and galaxies. For a given values of total $N(\mathrm{H\ I})$ and metallicity (Z) we generate grids of models varying the density in the range, $-3 \leqslant \log n_{\rm H}(\mathrm{cm}^{-3}) \leqslant 1.5$. The results of our model calculations are summarized in Figs. 6 and 7. From
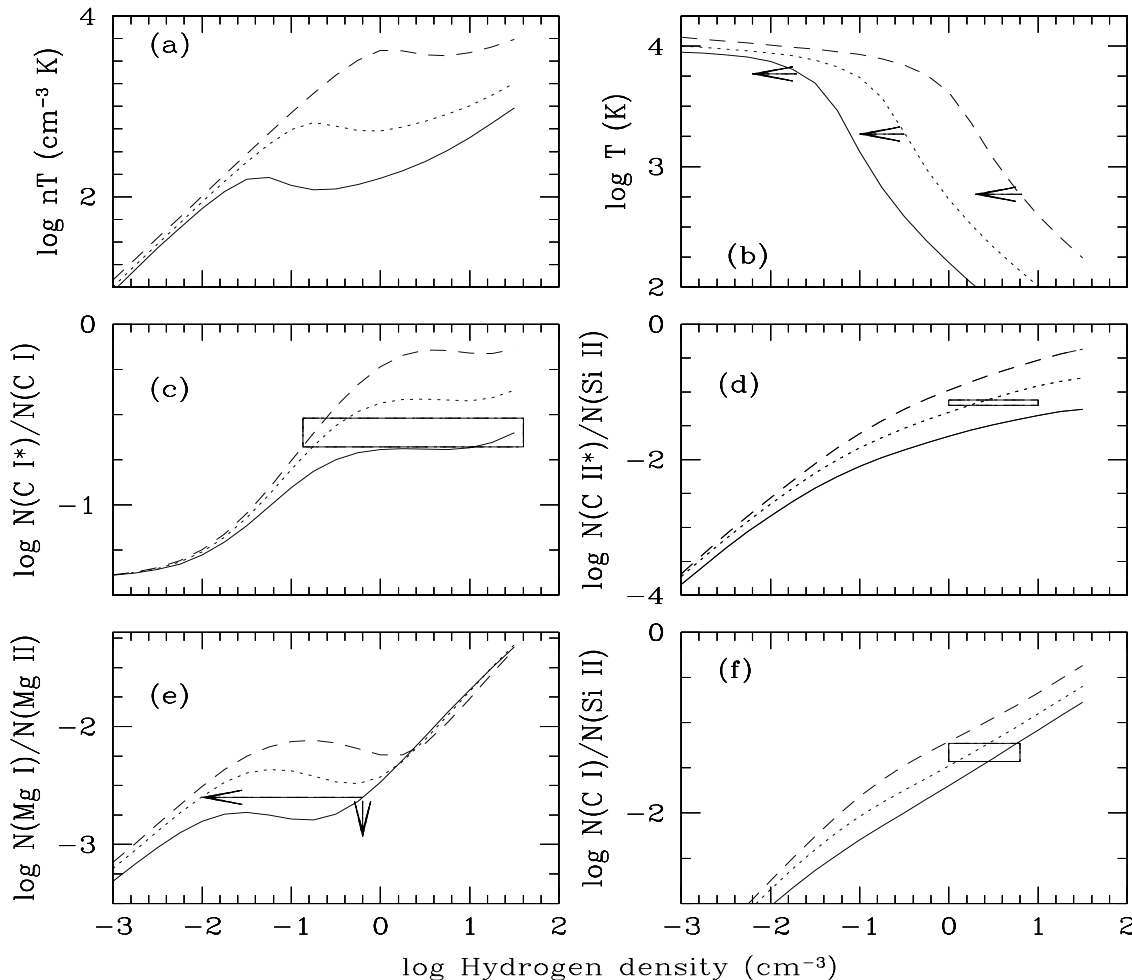
Figure 6. Results of photoionization models. The solid, short-dashed and long-dashed curves are for, respectively, log N(H I) = 20.0, 19.5 and 19.0. Metallicity is 0.5 Z$_\odot$. Constraints from the observed ratios of column densities integrated along the line of sight are shown in each panel as boxes or arrows. The arrows in panel (b) indicate the upper limits on n_H obtained from the upper limit on the 21-cm optical depth assuming the spin temperature to be equal to the kinetic temperature and complete coverage of the background radio source.

these figures it can be seen that, for the range of N(H I) considered here, most of the constraints are consistent with $0 \leqslant \log[n_H$ (cm^{-3})] $\leqslant 1$. This density range corresponds to the gas being part of a CNM phase ($T < 100$ K) only for the model with log N(H I) = 20 (see panel (a) of Fig. 6). In the other two models, that have N(H I) consistent with the observed range, the gas has the characteristics of a WNM phase or is in the thermally unstable region. Therefore, it seems most likely that the C I absorption is originating either from WNM or WIM. The N(Mg I)/N(Mg II) ratio predicted by these models is larger than the observed ratio. This can be explained by the large uncertainties in N(Mg II) due to heavy saturation of the absorption lines (see Fig. 1).

The models allow us to estimate metallicity and depletion. From Fig. 7 it is clear that for $-1 \leqslant \log n_H$(cm^{-3}) $\leqslant 1$ the ionization corrections for H I, O I, Mg II and Si II are negligible. Thus these ionization states can be used di-

rectly to infer the overall metallicity of the system. For N(H I)$\simeq 10^{19.5}$ cm^{-2} the observed column density of Si II and the lower limits on O I and Mg II column densities are consistent with Z = 0.56 Z$_\odot$. For such a metallicity the predicted column densities of Fe II and Mn II are about an order of magnitude higher than the observed column densities. The lower gas-phase abundance of Iron co-production elements with respect to the $\alpha-$process elements is confirmed by the measured low column density of Cr II and the absence of Ni II absorption. If this difference is due to depletion onto dust, then predictions for the Zn II column density should match the observed value. This is not the case and Zn II is overpredicted by the models. This argues toward an excess of $\alpha-$process elements.

Before drawing strong conclusions on the physical state of the gas, size of the absorbing region and the metal enrichment scenario it may be interesting to investigate the
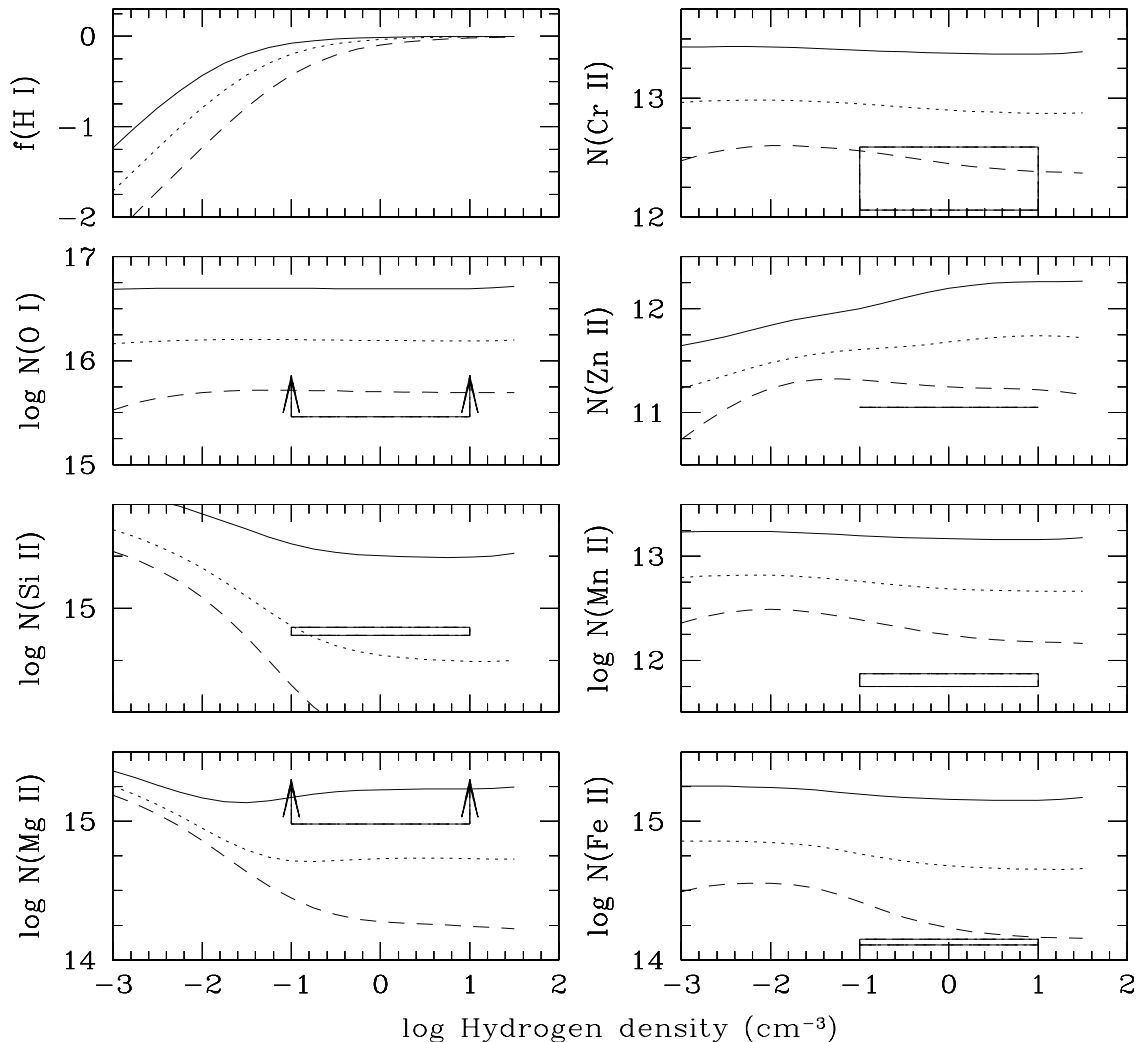
Figure 7. Results of photoionization models. Various ion column densities predicted by the models are plotted as a function of hydrogen density. Symbols are as in Fig. 6. $f(\mathrm{H\,I}) = N(\mathrm{H\,I})/N(\mathrm{H})$.

physical state of C I sub-components. While single cloud models give the average property of the gas, modelling individual velocity ranges will allow us to investigate variations of physical conditions across the profile. In the following Section we therefore discuss properties of the different C I velocity ranges we have identified before (see Fig. 1). In the corresponding models we have varied $N(\mathrm{H\,I})$ from 10^{18} to 10^{19} cm^{-2}.

4.1 Discussion on the different velocity ranges

4.1.1 Velocity range A

This velocity range has three well resolved components and an additional weak component in the red wing. C I absorption is possibly present in the three main components with little C I* absorption. We find that the upper limit on

$N(\mathrm{C\,I}^*)$ is consistent with log $n_{\mathrm{H}}(\mathrm{cm}^{-3}) \leqslant 0.0$ for models with log $N(\mathrm{H\,I}) \leqslant 19$. C II* absorption is blended with a strong Ly-α line at $z_{\mathrm{abs}} = 1.5$. Therefore, there is no strong constraint on the density for this velocity range. This velocity range has log $N(\mathrm{Mg\,I})/N(\mathrm{Mg\,II}) \simeq -2.4$ and log $N(\mathrm{O\,I})/N(\mathrm{Si\,II}) = 0.06 \pm 0.05$. In our model calculations these ratios are consistent with log $N(\mathrm{H\,I}) \leqslant 18.5$ and $-3 \leqslant \log n_{\mathrm{H}} \ (\mathrm{cm}^{-3}) \leqslant -2.0$. Such low densities are needed to explain that $N(\mathrm{O\,I})/N(\mathrm{Si\,II})$ is different from [O/Si]. We also find that the observed log $N(\mathrm{Al\,III})/N(\mathrm{Al\,II}) = -0.22 \pm 0.11$ ratio is consistent with low $N(\mathrm{H\,I})$ and low density. The presence of possible additional local radiation below the Lyman limit from the local stellar population would reproduce the observed $N(\mathrm{Mg\,I})/N(\mathrm{Mg\,II})$ ratio at higher densities (Fig. 9). In any case models for this gas require large ionization corrections for H I (see Fig. 7). We therefore do not
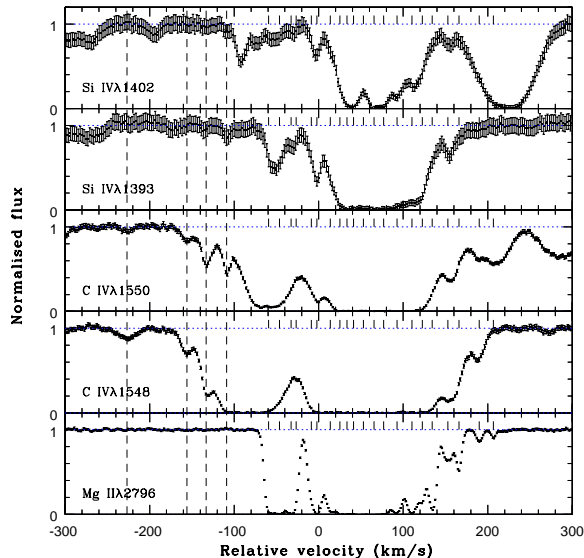
Figure 8. Profiles of high-ionization lines detected at $z_{abs}=$ 1.3647. Tick marks indicate the location of the different velocity components seen in the low-ionization profiles. Vertical dashed-lines mark the location of components that are detected only in the high ionization species.

Table 3. Model results for the velocity range B

Species	log N (Observed)	log N(H I) = 19.0−18.5	
		Z = 0.1 Z$_\odot$	Z = 0.5 Z$_\odot$
C I	12.92±0.01	11.99−12.14	12.66−12.84
C I*	12.56±0.02	11.28−11.60	11.95−12.30
C II*	13.30±0.03	12.14−12.38	12.81−13.06
O I^a	14.23±0.05	14.24−14.72	14.94−15.42
Mg I	11.37±0.01	11.50−11.74	12.08−12.31
Mg II^a	13.50±0.01	13.40−13.77	14.06−14.44
Al II	12.22±0.01	12.41−12.85	13.05−13.47
Si II	13.77±0.01	13.48−13.93	14.30−14.45
Fe II	13.07±0.01	13.30−13.70	13.99−14.42
Mn II	10.93±0.07	11.25−11.67	11.98−12.39
Zn II	10.61±0.20	10.34−10.66	10.99−11.30
Cr II	$\leqslant 11.30^b$	11.37−11.80	12.16−12.56

^{a} probably saturated; ^{b} 3σ upper limit.

attempt to further infer metallicities and depletion pattern in this velocity range.

4.1.2 Velocity range B

This velocity range has two components (one main component and a weak blend in the blue wing) and is associated with the strongest C I and C II* absorptions. From Fig. 1 it appears that the O I absorption is not heavily saturated. This velocity range contributes about ∼20% of the total N(O I). This means that about 20% of the total N(H I) is in this velocity range and N(H I) is probably not much higher than 10^{19} cm^{-2}. The observed log N(O I)/N(Si II) = 1.03±0.13 and log N(O I)/N(Mg II) = 1.30±0.16 ratios are consistent with solar metallicity ratios [O/Si]$_\odot$ = 1.13 and

[O/Mg]$_\odot$ = 1.11. As all these species are $\alpha-$process elements it is most likely that ionization corrections are negligible.

The measured N(C I*)/N(C I) is consistent with $-1.0 \leqslant \log[n_H(\mathrm{cm}^{-3})] \leqslant -0.6$ for $18 \leqslant \log [N(\mathrm{H\ I}) (\mathrm{cm}^{-2})] \leqslant 19.5$. The temperature of the gas is higher than 1000 K for the range in metallicity and log N(H I) considered here. The gas pressure in this component is consistent with $3.0 \leqslant \log[P/k(\mathrm{cm}^{-3}K)] \leqslant 3.6$. The gas is therefore warm with a neutral hydrogen fraction $\geqslant 0.7$.

The observed N(C II*)/N(Si II) ratio is much higher than that predicted by the models in the range of n_H derived from N(C I*)/N(C I). The difference is higher for higher N(H I) models. In Table. 3 we give the column densities of different species predicted in our model for $-1.0 \leqslant \log[n_H(\mathrm{cm}^{-3})] \leqslant -0.6$, $18.5 \leqslant \log [N(\mathrm{H\ I}) (\mathrm{cm}^{-3})] \leqslant 19$ and two different assumed values of metallicities (Z = 0.1 and 0.5 Z$_\odot$). From this table it is clear that the observed column densities of Si II, Mg II, Zn II and O I are well reproduced by the models with Z = 0.1 Z$_\odot$. However, the observed column densities of C I, C I* and C II* are higher than in the models. Also the well measured column densities of Fe II and Mn II are a factor of two below the model predictions. Models with Z $\geqslant$ 0.5 Z$_\odot$ are needed to explain N(C I) and N(C II*). These models will require a depletion of O, Mg, Al and Si by up to 0.6 dex and Fe, Mn and Cr by up to 1.0 dex.

The observed ratio, log N(Al III)/N(Al II) = $-0.15 \pm$ 0.17, is similar to what is observed for component A. This clearly suggests the presence of low-density ionized gas (with low column density) over the same velocity range as the C I gas. This is confirmed by the presence of strong Si IV and C IV absorption lines with similar velocity structure (see Fig. 8). It is interesting to note that the observed N(Mg I)/N(Mg II) ratio is explained by the models discussed here. This means that there is no excess of UV radiation with energies less than 13.6 eV in these velocity components (see Fig. 9). In conclusion this velocity range seems to be well apart from any local star-forming region, has metal enrichment between 0.1 and 0.5 Z$_\odot$ and reasonable depletion of iron co-production elements.

4.1.3 Velocity range C

This velocity range has $\geqslant$ 60% of the total O I column density distributed in 4 distinct velocity components. Only two of them show detectable C I* absorption and other two components are mainly in the wings of the absorption. Clearly most of the neutral hydrogen in the system must originate from this velocity range. The total column densities of C I, C I* and C II* in this velocity range are consistent with that seen for velocity range B. This means that the average pressure in both the velocity ranges are more or less consistent with one another. The measured N(C I*)/N(C I) ratio is consistent with $-1.0 \leqslant \log[n_H(\mathrm{cm}^{-3})] \leqslant -0.2$ for the range of N(H I) considered in our models. We also find that the models with $18.5 \leqslant \log [N(\mathrm{H\ I})(\mathrm{cm}^{-2})] \leqslant 19$ will also reproduce the observed N(C II*)/N(Si II) ratio. This means that we do not require enhancement of C with respect to Si and Mg as in component B. The gas pressure in this velocity range is $3.0 \leqslant \log[P/k(\mathrm{cm}^{-3}K)] \leqslant 3.8$. Like in velocity range B, the C I absorption from this component comes from a WIM or WNM.
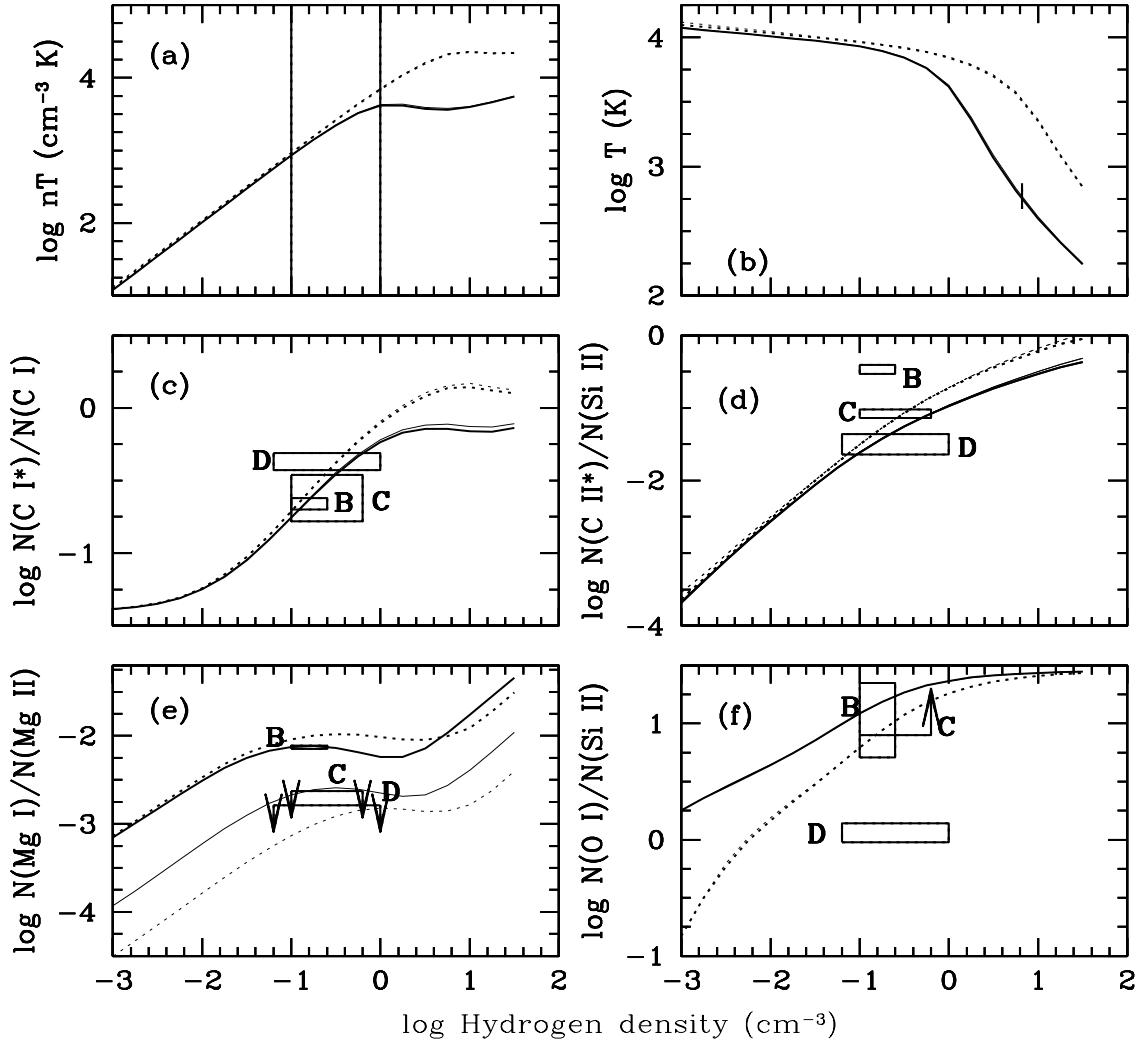
Figure 9. Results of photoionization models with an excess of local radiation in addition to the meta-galactic UV background radiation. Solid and dashed lines are for, respectively, log $N(\text{H I}) = 19.0$ and 18.5. Thick and thin curves are for models with and without local radiation added to the meta-galactic background radiation.

O I and Mg II absorptions are saturated and the derived column densities of Si II, Al II, Fe II, Mn II and Cr II are higher than in velocity range B. The column densities of C I, C II*, O I, Si II and Mg II are approximately consistent with $Z \geqslant 0.5\ Z_\odot$ (see Table 4). However the observed column densities of Fe II, Mn II and Cr II and the 3 σ upper limits on Ca II and Ni II are consistent with the iron co-production elements being under abundant by $\simeq 0.4$ dex. This depletion of iron co-production elements with respect to $\alpha-$elements is consistent with what is seen in the velocity range B.

As we have only a lower limit on the Mg II column density, the actual $N(\text{Mg I})/N(\text{Mg II})$ ratio may be smaller than that seen in velocity range B. From panel (e) in Fig. 9 it is clear that for log $N(\text{H I}) = 19$, the observed log $N(\text{Mg I})/N(\text{Mg II})$ ratio is consistent with a UV radiation field as high as the galactic mean UV field below 13.6 eV.

However, the observed $N(\text{Mg I})$ and $N(\text{C I})$ are inconsistent with much larger radiation fields (of the order of 10 times the Galactic field) as required for the H_2 components in high-z DLAs.

Like in the case of velocity range B we notice that the Al III column density is similar to that of Al II (log $N(\text{Al III})/N(\text{Al II}) = -0.04 \pm 0.02$). Also very strong Si IV and C IV absorptions are present with similar velocity structure as the low ionization lines (see Fig. 8). This again suggests that highly ionized gas is co-spatial with the C I component in this velocity range as well.

4.1.4   Velocity range D

The O I absorption in this velocity range is not saturated. However, Mg II lines are saturated (see Fig. 1). Only one out

Table 4. Model Results for the velocity range C

Species	N (Observed)	log N(H I) = 19.0−18.5 Z = 0.1 Z$_\odot$	Z = 0.5 Z$_\odot$
C I	12.97±0.02	12.04−12.14	12.66−12.88
C I*	12.65±0.10	11.28−11.98	11.94−12.54
C II*	13.35±0.03	12.14−12.47	12.81−13.13
O I[a]	⩾ 15.23	14.22−14.72	14.92−15.42
Mg I	11.97±0.01	11.43−11.74	11.99−12.31
Mg II[a]	⩾ 14.59	13.30−13.77	13.98−14.44
Al II	13.08±0.01	12.29−12.85	12.95−13.47
Si II	14.43±0.01	13.37−13.93	14.04−14.45
Ca II	⩽ 12.00[b]		12.45−12.68
Mn II	11.53±0.04	11.20−11.67	11.91−12.39
Fe II	13.65±0.03	13.23−13.70	13.90−14.42
Ni II	⩽ 12.95[b]		12.76−13.34
Zn II	⩽ 11.10[b]	10.28−10.66	10.94−11.30
Cr II	11.63±0.14	11.34−11.80	12.11−12.56

[a] probably saturated; [b] 3σ upper limit.

Table 5. Model results for range D

Species	N (Observed)	log N(H I) = 18.0 Z = 0.5 Z$_\odot$
C I	12.86±0.01	12.47−12.53
C I*	12.34±0.02	11.65−12.52
C II*	12.85±0.07	12.60−12.92
O I[a]	14.41±0.04	14.43
Mg I	11.64±0.01	11.75−12.17
Mg II[a]	⩾ 14.43	13.70−14.25
Al II	13.08±0.01	12.67−13.38
Si II	14.35±0.01	13.76−14.45
Fe II	13.50±0.03	13.59−13.97

[a] probably saturated; [b] 3σ upper limit.

of the three components show detectable C I* absorption. All components have N(O I)$\simeq N$(Si II) within 0.2 dex. For models considered here, N(C I*)$/N$(C I) and N(C II*)$/N$(Si II) are consistent with, $-1.2 \leqslant \log[n_{\mathrm{H}}(\mathrm{cm}^{-3})] \leqslant 0.0$ and $2.7 \leqslant \log[P/k(\mathrm{cm}^{-3}\mathrm{K})] \leqslant 3.8$.

Models predict log N(O I)$/N$(Si II)$\geqslant$ 0.9 for log N(H I) $\geqslant$ 18.5. Therefore observations are either consistent with log N(H I)<18.5 or require under-abundance of O with respect to Si. It can be seen from Table 5 that most of the column densities of singly ionized species can be reproduced by models with log N(H I) = 18 and Z = 0.5 Z$_\odot$.

4.2 Discussion

Rao & Turnshek (2000) have shown that DLAs can be pre-selected based on the equivalent widths of Mg II, Fe II and Mg I absorption lines. Specifically, they have found that 50% of the absorbers with rest equivalent width of Fe IIλ2600 and Mg IIλ2796 greater than 0.5 Å were confirmed DLAs. If they impose the condition W(Mg I)$\geqslant$ 0.5 Å then all the systems are confirmed DLAs. It is also clear from Fig. 3.4 of Lane's PhD thesis (2000) that 50% of these systems will be detected by 21-cm absorption. The inferred low N(H I) from IUE data (log N(H I) $\sim$ 19.3) and the absence of 21-cm absorption at z_{abs}= 1.3647 towards PKS 0237-233 are both

consistent with the above findings as W_{r}(Mg I)$\simeq$0.3Å in this system which is clearly a sub-DLA. It is therefore somewhat surprising to have found a wide-spread C I absorption associated with the system suggesting high metallicity. Wide-spread (i.e $\Delta V \geqslant 100$ km s^{-1}) C I absorption is seen at z_{abs}= 1.973 towards Q 0013−004 (Petitjean, Srianand & Ledoux 2002) and z_{abs}= 1.962 towards Q 0551−366 (Ledoux, Srianand & Petitjean 2002). Molecular hydrogen is detected in these systems although several of the C I components do not have associated H$_2$ absorption. C I absorption associated with H$_2$ have been shown to originate mainly from CNM gas (Srianand et al. 2005). However the nature of the gas in the components that do not have associated H$_2$ absorption is still unclear.

In the case of the z_{abs}= 1.365 system toward PKS 0237−233 a simple one cloud model can explain the total column densities. Under this assumption of single cloud, it can be shown that the gas producing C I absorption is most unlikely to be a CNM gas if the actual N(H I) is close to that we measure from the IUE spectrum. Detailed modelling of individual velocity ranges are also consistent with the gas responsible for the C I absorption in this system being either WNM or WIM. In addition we also infer ionization and chemical differences between individual velocity ranges.

Our GMRT observations give a good constraint on N(H I)$/T_{\mathrm{s}}$ if we assume complete coverage of the background radio-source by the absorbing gas. However, as pointed out before, the background radio source shows structures at milli-arcsec scale with a separation between the two brightest components of 85 pc at the absorption redshift. It is unclear which of these components coincides with the optical point source. If the brightest component that has most of the flux in the redshifted 21-cm range coincides with the optical source then we would have detected 21-cm absorption if the C I gas originates from the CNM. The non-detection would be a definite argument for the gas being warm. However, if the weaker radio component coincides with the optical source, then even if the C I absorption originates from CNM gas our GMRT observations would not be able to detect the corresponding 21-cm absorption as the expected size of the cloud is smaller than the radio source separation. It is known that strong Mg II systems (with W_{r} >0.3 Å) show coherent absorption over more than $\sim$ 2 kpc (Petitjean et al. 2000, Ellison et al. 2004). The fact that we find 21 distinct components along the line of sight to the optical point source means that it is likely that the overall system covers both the radio components. In that case our GMRT observations are consistent with no CNM with log N(H I)$\geqslant$ 19 along the radio source as well. Thus, it seems most likely that the region probed by the Mg II absorption system at z_{abs}= 1.365 is composed mostly of a warm neutral medium and/or warm ionized medium.

The inferred metallicities suggest that the gas has gone through an active star-formation period. We do find the signature of strong $\alpha-$process element enhancement with respect to Fe co-production elements. However, as we have not detected the Zn II absorption it is not clear, although unlikely, whether the difference could be attributed to dust-depletion. Photo-ionization models for the individual components are consistent with ionization by meta-galactic UV background. However, inconsistent with very large local ra-

diation field as one sees in H_2 components in high-z DLAs. This suggests that the system is, at the time of observation, in a low star-formation state.

Out of the 50 Mg II systems studied in the ESO large programme 'The Cosmic Evolution of the IGM', only two systems show C I absorption (i.e z_{abs}= 1.365 and 1.6724 towards PKS 0237−233). The only other sub-DLA towards radio quiet QSO HE 0001-2340 does not show C I and other fine-structure lines (See Richter et al. 2005). The inferred N(H I), metallicity, and depletion pattern at z_{abs}= 1.365 toward PKS 0237−233 are similar to what is observed at z_{abs}= 2.139 toward Tol 1037−2703. The latter system also shows detectable C I* and C II* absorption lines spread over $\sim$ 70 km s^{-1}and distributed in two distinct velocity components without detectable H_2 absorption. Interestingly the only other system that shows C I absorption in the large programme data is also found towards PKS 0237−2703. This line of sight is famous for the presence of a supercluster of C IV absorption lines. Thus, our study provides yet another motivation to go for further deep imaging and follow-up spectroscopic observations of the field (see Aragon-Salamanca et al. 1994).

ACKNOWLEDGEMENTS

REFERENCES

Abbott, D. C. 1982, ApJ, 263, 723
Aracil, B., Petitjean, P., Pichon, C. & Bergeron, J. 2004, A&A, 419, 811
Aragon-Salamanca, A., Ellis, R.S., Schwarzenberg, J.-M., Bergeron, J., 1994, ApJ, 421, 27
Ballester, P., Dorigo, K., Disaró, A., Pizarro de La Iglesia, J. A., Modigliani, A., & Boitquin, O., ASPC, 216, 461
Bahcall, J., Joss P. C., Lynds, R., 1973, ApJ, 182, 95
Bergeron, J., Petitjean, P., Aracil, B. et al. 2004, Msngr, 118, 40
Black, J. H. 1987, Interstellar processes, ed. Hollenbach, D. J., Thronson, H. A. (Dordrecht: Reidel), p731
Briggs, F. H., & Wolfe, A. M., 1983, ApJ, 268, 76
Briggs, F. H., Wolfe, A. M., Liszt, H. S. et al. 1989, ApJ, 341, 650
Carilli, C., Land, W., de Bruyn, A. G., Braun, R., & Miley, G. K. 1996, AJ, 112, 1317
Chand, H., Srianand, R., Petitjean, P., & Aracil, B. 2004, A&A, 417, 853
Curran, S. J., Murphy, M. T., Philstrom, Y. M., Webb, J. K., & Purcell, C. R. 2005, MNRAS,356, 1509

Dekker H., D'Odorico S., Kaufer A., Delabre B., & Kotzlowski H. 2000, in Iye M., Moorwood A. F., eds, Proc. SPIE Vol. 4008, Optical and IR telescope instrumentation and detectors, p. 534
Draine, B. T., & Bertoldi, F. 1996, ApJ, 468, 269
Edlén, B. 1966, Metrologia, 2, 71
Ellison, S. L., Ibata, R., Pettini, M., Lewis, G. F., Aracil, B., Petitjean, P. & Srianand, R. 2004, A&A, 414, 79
Ferland G. J., Korista, K. T., Verner, D. A., Ferguson, J. W., Kingdon, J. B., & Verner, E. M. 1998, PASP, 110, 761
Fey, A. L., Clegg, A. W., & Fomalont, E. B. 1996, ApJS, 105, 299
Fomalont, E. B., Frey, S., Paragi, Z. et al., 2000, ApJS, 131, 95
Ge, J., & Bechtold, J. 1999, in Carilli C. L., Radford S. J. E., Menten K. M., & Langston G. I., eds., Highly redshifted Radio Lines, ASP Conf. Series, Vol. 156, p. 121
Ge, J., Bechtold, J. & Black, J. H. A. 1997, ApJ, 434, 67
Haardt, F & Madau, P., 2005, Private communication.
Heinmüller, J., Patrick, P., Ledoux, C., Caucci, S., & Srianand, R. 2005, A&A, 449, 33
Jenkins, E. B., & Tripp, T. M. 2001, ApJ, 137, 297
Kanekar, N., & Chengalur, J., 2003, A&A, 399, 857
Lane W., 2000, PhD Thesis, University of Groningen (http://www.astron.nl/p/WSRT_thesis.htm)
Ledoux, C., Petitjean, P., & Srianand, R. 2003, MNRAS, 346,209
Ledoux, C., Srianand, R., & Petitjean, P., 2002, A&A, 392, 781
McKee. C. F., & Ostriker, J. P. 1977,ApJ, 218, 148
Meyer, D. M., Black, J. H., Chaffee, F. H., Foltz, G., & York, D., 1986, ApJ, 308, 37
Petitjean, P., Aracil, B., Srianand, R. & Ibata, R. 2000, A&A, 359, 457
Petitjean, P., Srianand, R., & Ledoux, C. 2000, A&A, 364, L26
Petitjean, P., Srianand, R., & Ledoux, C. 2002, MNRAS, 332, 383
Rao, S. M., & Turnshek, D. A. 2000, ApJS, 130, 1
Richter, P., Ledoux, C., Petitjean, P. & Bergeron, J. 2005, A&A, 440, 819
Roth, K. C., & Bauer, J. 1999, ApJ, 515, 57
Shaw, G., Ferland, G., Srianand, R., & Abel, N. 2006, ApJ, 639, 941
Silva, A. I., & Viegas, S. M. 2002, MNRAS, 329, 135
Songaila, A et al., 1994, Nature, 371, 43
Srianand, R., & Petitjean, P. 1998, A&A, 337, 51
Srianand, R., & Petitjean, P. 2001, A&A, 373, 816
Srianand, R., Petitjean, P., & Ledoux, C., 2000, Nature, 408, 931
Srianand, R., Petitjean, P., Ledoux, C., Ferland, G., & Shaw, G. 2005, MNRAS, 362, 549
Stumpff, P. 1980, A&AS, 41, 1
Viegas, S. M. 1995, MNRAS, 272, 35
Wolfe, A. M., & Briggs, F.H. 1981, ApJ, 248, 460
Wolfe, A. M., Briggs, F. H., Turnshek, D. A., Davis, M. M., Smith, H. E., & Cohen, R. D. 1985, ApJ, 294, L67
Wolfe, A. M. Prochaska, J. X., & Gawiser, E. 2003, ApJ, 593, 215
Wolfe, A. M., Gawiser, E., & Prochaska, J. X. 2003, ApJ, 593, 235
Wolfe, A. M., Howk, J. C., Gawiser, E., Prochaska, J. X., & Lopez, S. 2004, ApJ, 615, 525
Yamasaki, N. Y., Miyazaki, H., Ohashi, T., & Wilkes, B. 1998, PASJ, 50, 19